Electronic Supplementary Information (ESI) for

Zero-valent iron nanomaterial $Fe^0@Fe_2MnO_4$ for ultrasensitive electroanalysis of As(III): Fe^0 influenced surficial redox potential

Meng Yang,[a,b] Feng Xie,[b] Shan-Shan Li,[c,*] Chu-Hong Lin,[a,*] Xing-Jiu Huang[a,*], Wen-Qing Liu[b]

[a] Key Laboratory of Environmental Optics and Technology, And Environmental Materials and Pollution Control Laboratory, Institute of Solid State Physics, HFIPS, Chinese Academy of Sciences, Hefei 230031, China

[b] Anhui Institute of Optics and Fine Mechanics, Chinese Academy of Sciences, Hefei 230031, P.R. China

[c] Anhui Province Key Laboratory of Pollutant Sensitive Materials and Environmental Remediation, Department of materials science and engineering, Huaibei Normal University, Huaibei 235000, P.R. China

*Corresponding author

E-mail: xingjiuhuang@iim.ac.cn (X.J. Huang), chlin@iim.ac.cn (C.H. Lin), sa157002@mail.ustc.edu.cn (S.S. Li)

Tel.: +86-551-65591167; Fax: +86-551-65592420

1. Experimental Section and Discussion

1.1 Chemical Reagents. $Fe(acac)_3$, $Mn(acac)_3$, oleic acid (OA, 90%), sodium oleate (SO) and benzyl ether were purchased from Alfa Aesar, China. Anodized aluminum-oxide (AAO) membranes with pore widths of ~300 nm and lengths of ~60 μm were purchased from Shanghai Shangmu Technology Co. Ltd. N_2 (99.999%) was purchased from Chenghong Gas, Nanjing, China. All chemicals were used as received without further purification.

1.2 Synthesis of Fe_2MnO_4 Nanoparticles. We prepared the Fe_2MnO_4 nanoparticles in a similar way as previously reported work, but replaced $Co(acac)_2$ by $Mn(acac)_3$.[1] Firstly, 560 mg $Fe(acac)_3$, 254 mg $Mn(acac)_3$, 600 mg SO and 4 mL OA were dissolved in 20 mL benzyl ether in a 50 mL three-neck flask at room temperature. Then the mixture was heated to 120 ^oC for 1 h under N_2 flow. During this time, a process to remove water and oxygen is necessary. After that, the reaction mixture was heated to 290 ^oC for another 1 h with the protection of N_2. After cooling down to room temperature, the Fe_2MnO_4 nanoparticles was precipitated out by addition of ethanol and then re-dispersed in hexane with a concentration of 20 mg mL^{-1} for further using.

1.3 Fabrication of Monolayer Tubular $Fe^0@Fe_2MnO_4$ Nanoparticles. The self-assembly of nanoparticles into tubes is a reference to the work of Li *et al.*.[2] In general, the OA-functionalized anodic aluminum oxide (AAO) membrane was immersed in as-prepared Fe_2MnO_4 nanoparticles solution (~ 2 mL) in a small glass vial. Then put the glass vial into an oven with 80 ^oC. The self-assembly of Fe_2MnO_4 nanoparticles into tubes will proceed with the fast solvent evaporation. After the hexane completely evaporation, the AAO membrane containing the as-assembled monolayer Fe_2MnO_4 nanoparticles was calcined at 500 °C for 2 h in H_2/Ar (5% H_2), which can reduce Fe_2MnO_4 into $Fe^0@Fe_2MnO_4$ and carbonize the surface-coating OA ligands to a thin carbon shell. For comparison, the monolayer tubular Fe_2MnO_4 was synthesized under the calcination pure N_2. The final step is to remove the template of AAO using 6 M KOH. The product of carbon-covering monolayer tubular-$Fe^0@Fe_2MnO_4$ and -

Fe_2MnO_4 nanoparticles were obtained after wash with water several times.

1.4 Apparatus. Electrochemical measurements were performed with SPCEs (Screen-Printed Carbon Electrode, DeltBio, Shanghai, China). The electrochemical cell consists of a three-electrode arrangement with a SPCE (3 mm diameter) serving as the working electrode; carbon served as the counter electrode. A silver pseudo-reference electrode completes the circuit. All measurements were performed with a CHI 660D computer-controlled potentiostat (ChenHua Instruments Co., Shanghai, China). The SEM images were taken using a field-emission scanning electron microscope (FESEM, Quanta 200 FEG, FEI Company, USA). The transmission electron microscopy (TEM) and high resolution TEM (HRTEM) as well as EDS analyses were performed using a JEM-2010 transmission electron microscope operating at 200 kV (Quantitative method: Cliff Lorimer thin ratio section). The high angle annular dark field scanning transmission electron microscopy (HAADF-STEM) is operated on aberration-corrected scanning transmission electron microscope (Ac-STEM, JEOL ARM-200F). The X-ray diffraction (XRD) patterns of the samples were obtained with a Philips X'Pert Pro X-ray diffractometer with Cu Kα radiation (1.5418Å). X-ray photoelectron spectroscopy (XPS) measurements were operated using a VG ESCALAB MKII spectrometer with an Mg Ka X-ray source (1253.6eV, 120W) at a constant analyzer.

1.5 Fabrication of $Fe^0@Fe_2MnO_4$ Modified Screen-Printed Carbon Electrode. The synthesized $Fe^0@Fe_2MnO_4$ were added to water and ultrasonicated for 1 min to obtain a 0.3 mg mL^{-1} suspension. To fabricate the modified electrode, 7 μL of the suspension was pipetted onto the surface of the carbon working electrode in SPCE and evaporated under room temperature to obtain the $Fe^0@Fe_2MnO_4$ SPCE. For comparison, the Fe_2MnO_4 SPCE were prepared in the same way.

1.6 Electrochemical Test. The $Fe^0@Fe_2MnO_4$ nanoparticles modified screen-printed carbon electrode (SPCE) served as the working electrode for arsenic detection with square wave anodic stripping voltammetry (SWASV) under optimized conditions. The as-prepared $Fe^0@Fe_2MnO_4$ SPCE was dipped in a stirred analyte solution of 0.1

M HAc-NaAc (pH 5.0) containing As(III) and kept at −1.0 V for 120 s. The anodic stripping was performed from −0.5 to 0.6 V. After each measurement, the modified electrode was regenerated in a freshly stirred supporting electrolyte by desorption at 0.6 V for 120 s to remove the previous residual As(0) from the electrode surface. For comparison, other modified electrodes were used with the same processes and conditions.

1.7 Adsorption Experiments. The physical adsorption experiments: in order to be consistent with electrochemical sensing conditions, all the adsorption measurements were performed in 0.1 M HAc-NaAc (pH 5.0 ± 0.2). To start the experiment, 10 mg of the individual sorbent was introduced into 10 mL aqueous solution containing As(III) using a 15 mL centrifuge tube, and then the solutions were shaken at 298 K for 24 h to ensure the sorption process reach equilibrium. The water used here were all operated with the process of deoxygenated by N_2. The solid and liquid phases were separated by centrifugation at 4000 rpm for 3 min, and the solid was dried using freezing dryer with high vacuum for further XPS and HRTEM analysis. The adsorption experiments with negative potential (electro-adsorption): the process of electro-adsorption is the same as the electrochemical concentration process of detection. The modified electrodes were immersed in 0.1 M HAc-NaAc (pH 5.0) containing As(III) with applying −1.0 V for 120 s. Then take out of the electrode for further characterization of XPS analysis.

1.8 Evidence of Fe^0 Promoted Surface Fe(II)/Fe(III) Experiments. We study the structural differences between the $Fe^0@Fe_2MnO_4$ and Fe_2MnO_4 nanoparticles in detail by high-angle annular dark field-scanning transmission electron microscopy (HAADF-STEM). The adsorption experiments of As(III) on both $Fe^0@Fe_2MnO_4$ and Fe_2MnO_4 nanoparticles are all performed, including simple adsorption, adsorption with potential and stripping during the detection. We further show the valence and binding states change of As(III), O and Fe(III) on adsorption samples by X-ray photoelectron spectroscopy (XPS).

1.9 Simulation Method. The electrocatalytic reactions of A/B mediated by X/Y is expressed as Eqn. (1)-(4):

$$\mathrm{A(sol)} \underset{k_{\mathrm{des}}}{\overset{k_{\mathrm{ads}}}{\rightleftharpoons}} \mathrm{A(ads)} \quad \text{* MERGEFORMAT (1)}$$

$$\mathrm{A(ads)} + 3\mathrm{e}^- \underset{k_{\mathrm{AB\_ox}}}{\overset{k_{\mathrm{AB\_red}}}{\rightleftharpoons}} \mathrm{B(ads)},\ E_{\mathrm{f,AB}} \quad \text{* MERGEFORMAT (2)}$$

$$\mathrm{A(ads)} + \mathrm{X} \xrightarrow{k_{\mathrm{cat}}} \mathrm{B(ads)} + \mathrm{Y} \quad \text{* MERGEFORMAT (3)}$$

$$\mathrm{Y} + \mathrm{e}^- \underset{}{\overset{k_{\mathrm{XY}}}{\rightleftharpoons}} \mathrm{X},\ E_{\mathrm{f,XY}} \quad \text{* MERGEFORMAT (4)}$$

The mass transport of A(sol) is simply modelled by Fick's Second Law:

$$\frac{\partial c_{\mathrm{A(sol)}}}{\partial t} = D_{\mathrm{A(sol)}} \nabla^2 c_{\mathrm{A(sol)}} \quad \text{* MERGEFORMAT (5)}$$

Where c is the concentration, t is the reaction time and $D_{\mathrm{A(sol)}}$ is the diffusion coefficient. $D_{\mathrm{A(sol)}}$ is set as 10^{-7} $\mathrm{m^2 s^{-1}}$ considering that the solution is under stirring during the pre-concentration. As the aim of this model is to explore the influence of X/Y and it is seen from experimental data that the mass transport of A(sol) is not the rate-determining step, we set $D_{\mathrm{A(sol)}}$ a relatively large value.

The reaction rate equations determined by the adsorption of A(sol), the direct electron transfer of A/B, the mediated reduction of A and the electron transfer of X/Y are described as following:

$$-D_{\mathrm{A(sol)}} \nabla c_{\mathrm{A(sol)}} = -k_{\mathrm{ads}} c_{\mathrm{A(sol)}} + k_{\mathrm{des}} \Gamma_{\mathrm{A(ads)}} \quad \text{* MERGEFORMAT (6)}$$

$$\frac{\partial \Gamma_{\mathrm{A(ads)}}}{\partial t} = k_{\mathrm{ads}} c_{\mathrm{A(sol)}} - k_{\mathrm{des}} \Gamma_{\mathrm{A(ads)}} - k_{\mathrm{AB\_red}} \exp\left(-0.5 \frac{F\left(E - E_{\mathrm{f,AB}}\right)}{RT} \right) \Gamma_{\mathrm{A(ads)}} + k_{\mathrm{AB\_ox}} \exp\left(0.5 \frac{F\left(E - E_{\mathrm{f,AB}}\right)}{RT} \right) \Gamma_{\mathrm{B(ads)}} - k_{\mathrm{cat}} \Gamma_{\mathrm{A(ads)}} \Gamma_{\mathrm{X}} \quad \text{* MERGEFORMAT (7)}$$

$$\frac{\partial \Gamma_{\mathrm{B(ads)}}}{\partial t} = -k_{\mathrm{ads}} c_{\mathrm{A(sol)}} + k_{\mathrm{des}} \Gamma_{\mathrm{A(ads)}} + k_{\mathrm{AB\_red}} \exp\left(-0.5 \frac{F\left(E - E_{\mathrm{f,AB}}\right)}{RT} \right) \Gamma_{\mathrm{A(ads)}} - k_{\mathrm{AB\_ox}} \exp\left(0.5 \frac{F\left(E - E_{\mathrm{f,AB}}\right)}{RT} \right) \Gamma_{\mathrm{B(ads)}} + k_{\mathrm{cat}} \Gamma_{\mathrm{A(ads)}} \Gamma_{\mathrm{X}}$$ *

MERGEFORMAT (8)

$$\frac{\partial \Gamma_{\mathrm{X}}}{\partial t} = -\frac{\partial \Gamma_{\mathrm{Y}}}{\partial t} = -k_{\mathrm{cat}} \Gamma_{\mathrm{A(ads)}} \Gamma_{\mathrm{X}} + k_{\mathrm{el\_XY}} \exp\left(-0.5 \frac{F\left(E - E_{\mathrm{f,XY}}\right)}{RT} \right) \Gamma_{\mathrm{Y}} - k_{\mathrm{el\_XY}} \exp\left(0.5 \frac{F\left(E - E_{\mathrm{f,XY}}\right)}{RT} \right) \Gamma_{\mathrm{X}}$$ *

MERGEFORMAT (9)

E is the applied potential (V), *F* is the Faraday constant, *R* is the gas constant and *T* is the room temperature which we set as 298.15 K. The meaning of other parameters has been explained in the main text. We simulated the overall reaction procedure including a pre-concentration step and a stripping step. The electrochemical conditions set to the simulation model is the same as the optimum experimental conditions. Here we set the initial surface coverage of X to be 10^{-7} mol m^{-2} and during reaction the sum of X and Y is always 10^{-7} mol m^{-2}. Previous study reported that a 4 nm Fe_3O_4 nanoparticle has ca. 30 active iron sites.[3] The assumption of a 10^{-7} mol m^{-2} X in Figure 7b corresponds to a very low density of active sites (only 1 active site on a 4 nm-diameter nanoparticle).

1.10 Electrochemical Characterization and the Optimized Experimental Conditions. Before the detection, the electrochemical characterization and the optimized experimental conditions of the Fe^0@Fe_2MnO_4 SPCE are studied as presented in Fig. S8 and S9 (ESI†). Probing by cyclic voltammetry and electrochemical impedance spectra (Fig. S8, ESI†), the Fe^0@Fe_2MnO_4 SPCE exhibits a better conductivity than bare SPCE and Fe_2MnO_4, which benefits from the core Fe^0. The optimal conditions are determined as 0.1 M HAc-NaAc (pH 5.0) with -1.0 V for 120 s pre-concentration time and the electrode modified with 7 μL volume of 0.3 mg mL^{-1} Fe^0@Fe_2MnO_4 suspension (Fig. S9, ESI†).

1.11 Investigate on Stability and Reproducibility. Besides, the stability of Fe^0@Fe_2MnO4 nanoparticles is tested with 10 ppb As(III) for 15 consecutive and repetitive stripping (Fig. S14a). The relative standard deviation (RSD) is only 1.41%, which proves the stability of the fabricated electrode. We also examine three different Fe^0@Fe_2MnO_4 SPCE, the peak shape shows slight shift and the peak current is almost identical (Fig. S14b), indicating that the fabricated sensor has excellent reproducibility.

2. Figures

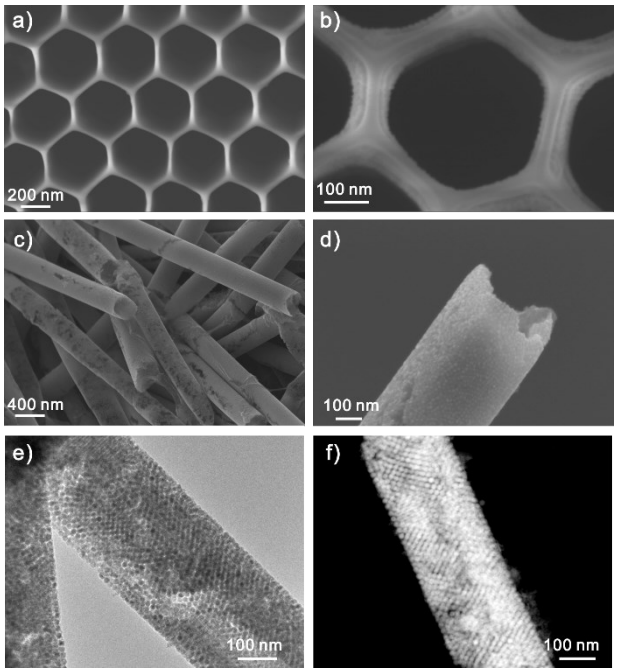

Fig. S1 Cross section images of the anodic aluminum oxide (AAO) template a) without and b) with self-assembled monolayer Fe_2MnO_4. c) Low-magnification scanning electron microscope (SEM) and d) high-resolution scanning electron microscope (HRSEM) images of as-synthesized Fe^0@Fe_2MnO_4. e) TEM and f) HAADF-STEM images of monolayer tubular Fe_2MnO_4.

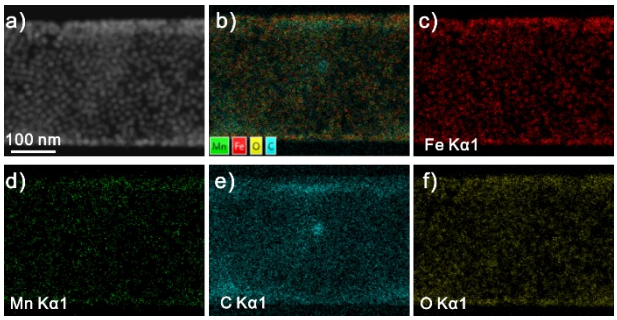

Fig. S2 a) HAADF-STEM image and b-f) the corresponding elemental energy dispersive spectrometer (EDS) mapping images of as-synthesized $Fe^0@Fe_2MnO_4$ nanoparticles.

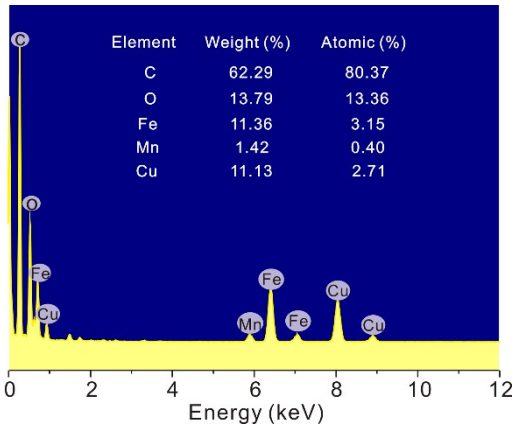

Fig. S3 EDS pattern of prepared $Fe^0@Fe_2MnO_4$.

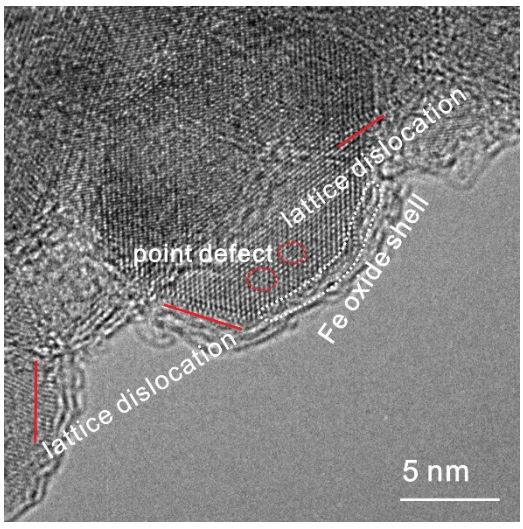

Fig. S4 HRTEM image of $Fe^0@Fe_2MnO_4$ nanoparticles.

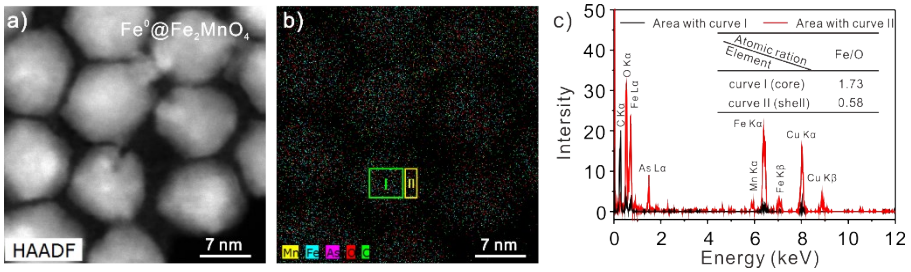

Fig. S5 a) HAADF-STEM image and b) the corresponding EDS elemental overlay image of $Fe^0@Fe_2MnO_4$ nanoparticles after adsorption of 1 ppm As(III). c) EDS spectra of core (i.e. the area in curve I of Figure j) and shell (curve II in Figure j) on $Fe^0@Fe_2MnO_4$ nanoparticles, inset is the atomic ratio of Fe and O.

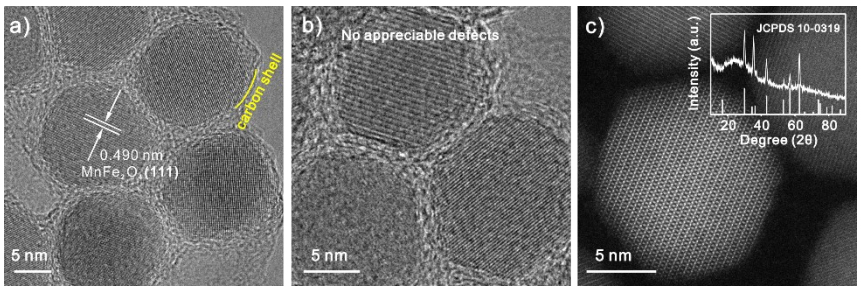

Fig. S6 a), b) HRTEM and c) HAADF-STEM image of Fe_2MnO_4 nanoparticles. Insets in c) is the corresponding X-ray diffraction (XRD) pattern.

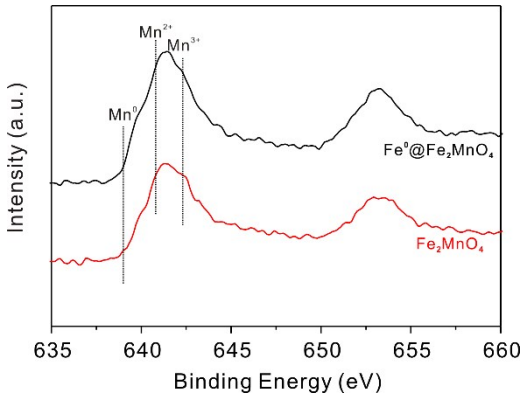

Fig. S7 High-resolution XPS spectra of Mn on the $Fe^0@Fe_2MnO_4$ and Fe_2MnO_4.

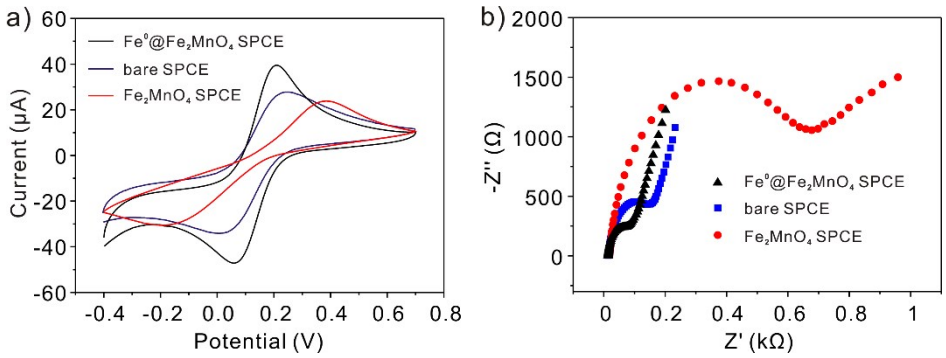

Fig. S8 a) Cyclic voltammograms and b) Nyquist diagram of electrochemical impedance spectra of the bare, $Fe^0@Fe_2MnO_4$ and Fe_2MnO_4 SPCE, respectively.

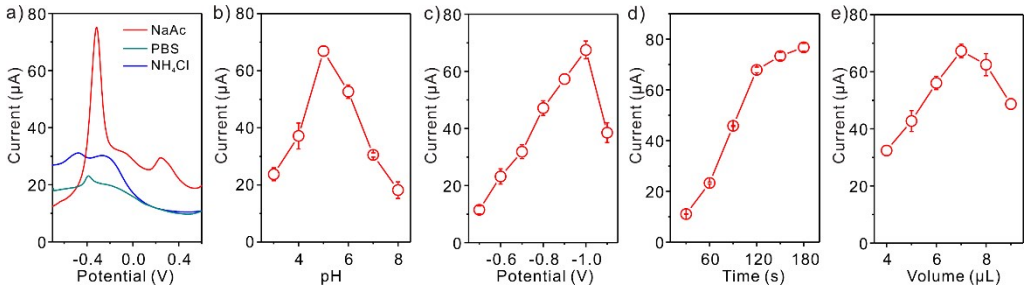

Fig. S9 Optimum the detection experimental conditions. Influence of a) supporting electrolytes; b) pH value; c) deposition potential; d) deposition time and e) modified volume on the response to 10 ppb As(III) on $Fe^0@Fe_2MnO_4$ SPCE.

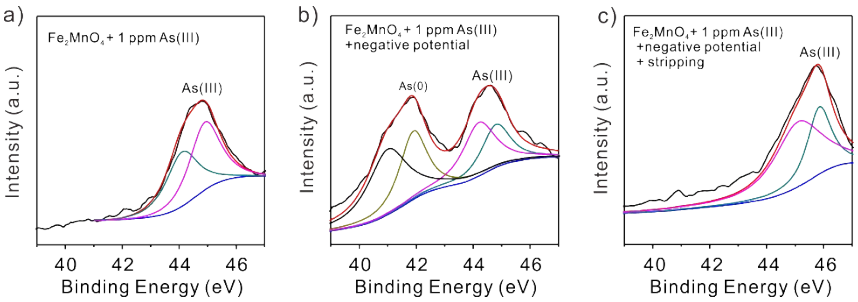

Fig. S10 High-resolution XPS spectra of As on Fe_2MnO_4 nanoparticles under different condition: a) with 1 ppm As(III) in solution, b) with applying negative potential, c) stripping after electro-adsorption.

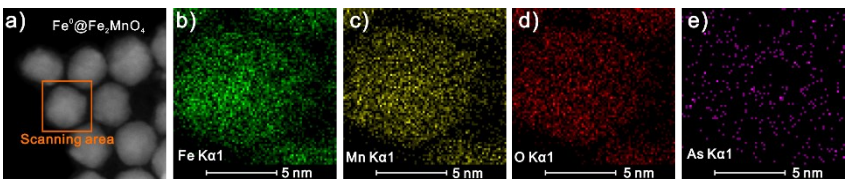

Fig. S11 a) HAADF-STEM image and corresponding EDS element maps of b) Fe, c) Mn, d) O and e) As of $Fe^0@Fe_2MnO_4$ nanoparticles after adsorption of 1 ppm As(III).

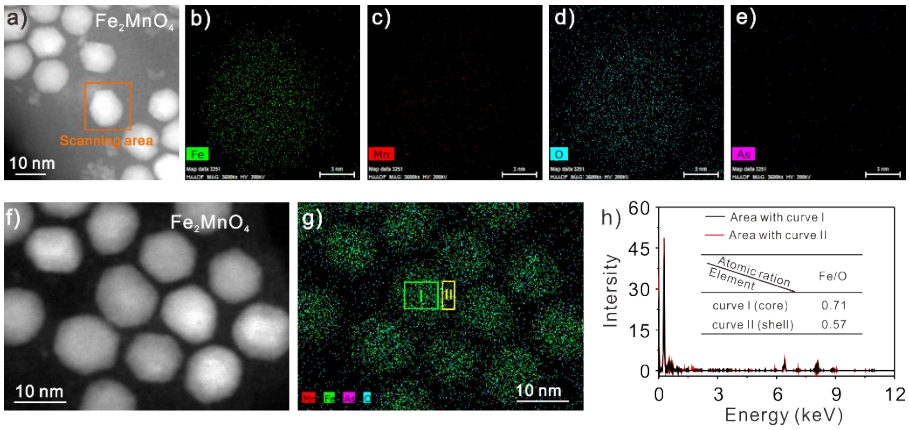

Fig. S12 a) HAADF-STEM image and corresponding EDS element mappings of b) Fe, c) Mn, d) O and e) As of Fe_2MnO_4 nanoparticles after adsorption of 1 ppm As(III). f) HAADF-STEM image and g) the corresponding EDS elemental overlay image of the four elements of Mn, Fe, As and O of Fe_2MnO_4 after adsorption of 1 ppm As(III). h) EDS spectra of core (i.e. the area in curve I of Figure g) and shell (curve II in Figure g) on Fe_2MnO_4, inset is the atomic ratio of Fe and O.

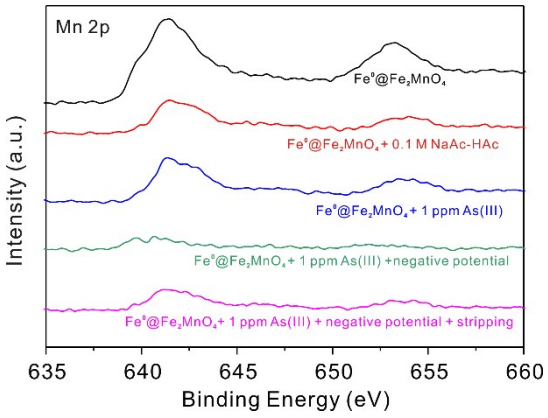

Fig. S13 High-resolution XPS spectra of Mn on $Fe^0@Fe_2MnO_4$, $Fe^0@Fe_2MnO_4$ in

HAc-NaAc for three days, with 1 ppm As(III) in solution, with applying negative potential and stripping after electro-adsorption.

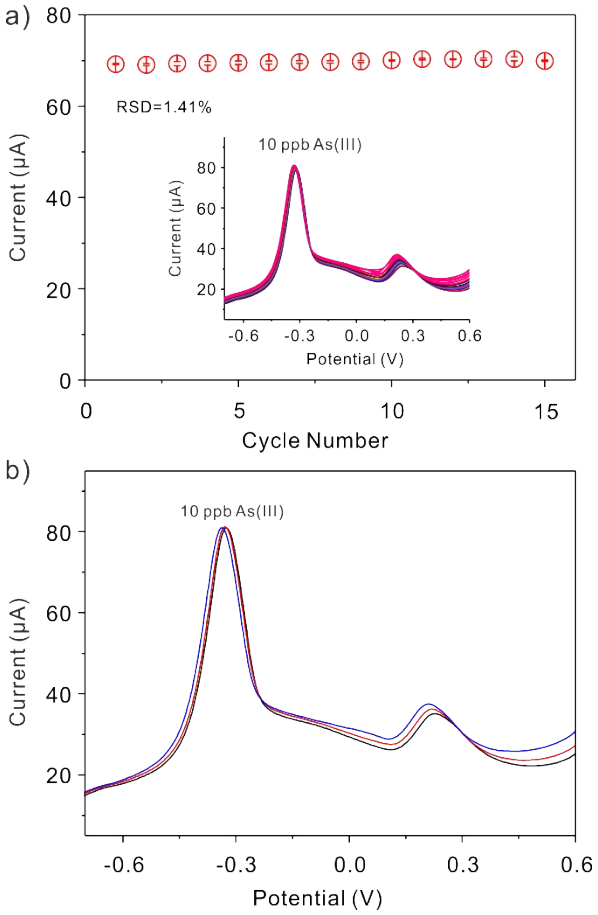

Fig. S14 a) Current change of 10 ppb of As(III) for 20 consecutive and repetitive stripping voltammetric measurements on the $Fe^0@Fe_2MnO_4$, inset is the corresponding SWASV response. b) The response of 10 ppb As(III) at three $Fe^0@Fe_2MnO_4$ SPCE after storage at room temperature for 30 days.

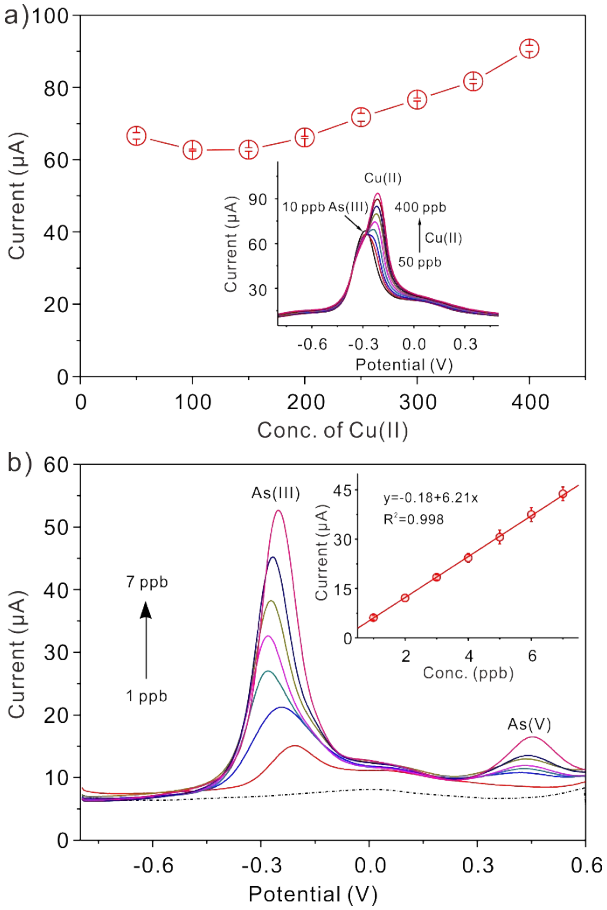

Fig. S15 a) The current change of 10 ppb As(III) in the addition of 50-400 ppb Cu(II) on $Fe^0@Fe_2MnO_4$ SPCE, inset is the corresponding SWASV response. b) The detection of As(III) in real sample with standard additions in the presence of 10 ppb Cu(II), inset is the corresponding linear calibration plot.

3. Table

Table S1. A comparison of detection performance of the Au-based (electro)chemical sensors for the analysis of As(III).

Electrode	Electrolyte (pH)	Linear range (ppb)	Sensitivity (μA ppb^{-1})	LOD (ppb)	Ref.
Au-coated BDD	1 M HCl	0.1–40	–	0.005	4
Au-UMEA	2 M HCl	0−500	0.044	0.013	5
Au-NEE	1 M HCl	0–3	3.14	0.02	6
sonically assisted gold microdisk electrode	0.1 M HNO_3	7.5−75	0.363	0.278	7
Au(111)-like polycrystalline gold electrode	0.1 M PBS (pH 1.0)	0−1125	0.3636	0.28	8
MWCNTs/gold electrode	0.1 M acetic bu□er (pH 4.0)	10−50	0.236	_	9
Au NPs/GCE	1 M HNO_3	0.5−15	0.024	0.25	10
Au NPs/GCE	0.1 M PBS + 0.01 M EDTA (pH 5.0)	0.1−15	0.21	0.0025	11
Au NPs/GCE	1 M HCl	0−7.5	0.24	0.0096	12
Au NPs-SPE	1 M HCl	0–250	–	0.4	13
3D Au nanodendrite network	0.2 M HCl	0.1–70	0.046	–	14
Au/Te GCE	1 M HCl	0.1–10	6.35	0.0026	15
AuNPs-CNTs	0.1 M HCl	0.75–7.5	26.5	0.1	16
CNT/AuNPs-GC/GCE	1 M H_2SO_4	7.5–375	0.08	2.5	17
FePt bimetallic	10 mM PBS	1−15	0.42	0.8	18
Au/carbon Films	0.1 M PBS	1−100	0.026	0.55	19
Ru NPs/GC	Clark-Lubs buffer(pH 2.0)	0−60	0.00238	0.1	20
Graphite-Au NPs	1 M HNO_3	1−50	4.6×10^{-6}	0.58	21
Fe_3O_4-RTIL/SPCE	0.1 M acetate bu□er (pH 5.0)	1−10	4.91	0.0008	22
Au/Fe_3O_4-RTIL/SPCE	0.1 M PBS (pH 5.0)	0.1−1; 1−10	4.54; 0.86	0.0022	23
Dumbbell-like Au/Fe_3O_4 SPCE	0.1 M acetate bu□er (pH 5.0)	0.1−10	9.43	0.0215	24
GSH-AuNPs	_	0−1	_	0.12	25
TMT-Au NPs	_	0−100	_	0.87	26

Tubular SPCE	$Fe^0@Fe_2MnO_4$	0.1 M acetate bu□er (pH 5.0)	1−15	6.32	0.053	This work

Table S2. Simulation parameters used in Figure 4

Variable	**Case 1**	**Case 2**	**Case 3**	**Case 4**
k_{ads}	$1.0x10^{-4}$	$1.0x10^{-2}$	$1.0x10^{-2}$	$1.0x10^{-2}$
k_{des}	1.0	1.0	1.0	1.0
k_{AB_red}	$1.0x10^{-7}$	$1.0x10^{-7}$	$1.0x10^{-7}$	$1.0x10^{-7}$
k_{AB_ox}	0.1	0.1	0.1	0.1
$E_{f,AB}$	-0.3	-0.3	-0.3	-0.3
k_{cat}	0	0	$1.0x10^{-4}$	$1.0x10^{-4}$
k_{XY}	0.1	0.1	0.1	0.1
$E_{f,XY}$	0	0	-0.6	0

4. References

1 L. H. Wu, P. O. Jubert, D. Berman, W. Imaino, A. Nelson, H. Y. Zhu, S. Zhang, S. H. Sun, *Nano Lett.,* 2014, **14**, 3395-3399.

2 T. T. Li, B. Xue, B. W. Wang, G. N. Guo, D. D. Han, Y. C. Yan, A. G. Dong, *J. Am. Chem. Soc.,* 2017, **139**, 12133-12136.

3 J. J. P. Roberts, J. A. Westgard, L. M. Cooper, R. W. Murray, *J. Am. Chem. Soc.,* 2014, **136**, 10783-10789.

4 Y. Song, G. M. Swain, *Anal. Chem.,* 2007, **79**, 2412-2420.

5 R. Feeney, S. P. Kounaves, *Anal. Chem.,* 2000, **72**, 2222-2228.

6 B. K. Jena, C. R. Raj, *Anal. Chem.,* 2008, **80**, 4836-4844.

7 A. O. Simm, C. E. Banks, R. G. Compton, *Anal. Chem.,* 2004, **76**, 5051-5055.

8 M. R. Rahman, T. Okajima, T. Ohsaka, *Anal. Chem.,* 2010, **82**, 9169-9176.

9 A. Profumo, M. Fagnoni, D. Merli, E. Quartarone, S. Protti, D. Dondi, A. Albini, *Anal. Chem.,* 2006, **78**, 4194-4199.

10 E. Majid, S. Hrapovic, Y. L. Liu, K. B. Male, J. H. T. Luong, *Anal. Chem.,* 2006, **78**, 762-769.

11 H. H. Chen, J. F. Huang, *Anal. Chem.,* 2014, **86**, 12406-12413.

12 X. Dai, O. Nekrassova, M. E. Hyde, R. G. Compton, *Anal. Chem.,* 2004, **76**, 5924-5929.

13 M. Khairy, D. K. Kampouris, R. O. Kadara, C. E. Banks, *Electroanalysis,* 2010, **22**, 2496-2501.

14 T. N. Huan, T. Ganesh, K. S. Kim, S. Kim, S. H. Han, H. Chung, *Biosensors & Bioelectronics,* 2011, **27**, 183-186.

15 D. M. Wang, Y. W. Zhao, H. L. Jin, J. X. Zhuang, W. M. Zhang, S. Wang, J. C. Wang, *ACS applied materials & interfaces,* 2013, **5**, 5733-5740.

16 L. Xiao, G. G. Wildgoose, R. G. Compton, *Anal. Chim. Acta,* 2008, **620**, 44-49.

17 X. Dai, G. G. Wildgoose, C. Salter, A. Crossley, R. G. Compton, *Anal. Chem.,* 2006, **78**, 6102-6108.

18 N. Moghimi, M. Mohapatra, K. T. Leung, *Anal. Chem.,* 2015, **87**, 5546-5552.

19 D. Kato, T. Kamata, D. Kato, H. Yanagisawa, O. Niwa, *Anal. Chem.,* 2016, **88**,

2944-2951.

20 R. Gupta, J. S. Gamare, A. K. Pandey, D. Tyagi, J. V. Kamat, *Anal. Chem.,* 2016, **88**, 2459-2465.

21 J. P. Mafa, N. Mabuba, O. A. Arotiba, *Electroanalysis,* 2016, **28**, 1462-1469.

22 C. Gao, X. Y. Yu, S. Q. Xiong, J. H. Liu, X. J. Huang, *Anal. Chem.,* 2013, **85**, 2673-2680.

23 J. Wei, S. S. Li, Z. Guo, X. Chen, J. H. Liu, X. J. Huang, *Anal. Chem.,* 2016, **88**, 1154-1161.

24 S. S. Li, W. Y. Zhou, M. Jiang, Z. Guo, J. H. Liu, L. Z. Zhang, X. J. Huang, *Anal. Chem.,* 2018, **90**, 4569-4577.

25 B. Zheng, J. Li, Z. Zheng, C. Zhang, C. Huang, J. Hong, Y. Li, J. Wang, *Opt. Laser Technol.,* 2021, **133**, 106522.

26 J. Li, L. Yang, Y. Ruan, S. Chu, H. Wang, Z. Li, C. Jiang, B. Liu, L. Yang, Z. Zhang, *ACS Appl. Nano Mater.,* 2020, **3**, 8224-8231.